Compact Omnidirectional Circularly Polarized Antenna via Alford Loop and Wire-Patch Structure Combination

FRANCESCO POSITANO (Graduate Student Member, IEEE), LUCA SANTAMARIA (Member, IEEE), ROBERT STARAJ (Member, IEEE), AND LEONARDO LIZZI (Senior Member, IEEE)

Université côte d'Azur, CNRS, LEAT, Sophia Antipolis 06410, France

CORRESPONDING AUTHOR: L. LIZZI (e-mail: leonardo.lizzi@univ-cotedazur.fr)

ABSTRACT A compact single-fed omnidirectional circularly polarized (OCP) antenna is presented. The circular polarization is obtained by combining an Alford Loop (AL) and a Wire-Patch (WP) radiating structures, which are used to generate two orthogonal E-field components. The antenna exhibits a clear right-handed circular polarization (RHCP) with a dipole-like omnidirectional radiation pattern. A prototype has been realized using two FR-4 printed circuit boards (PCBs) and experimentally tested. The measured overlapped -10 dB impedance matching and 3 dB axial ratio bandwidth is 120 MHz wide (4.9%) from 2.40 to 2.52 GHz. The measured RCHP maximum realized gain and total efficiency are 1.91 dBic and 87%, respectively. Its compact size ($0.25\lambda \times 0.25\lambda \times 0.08\lambda$), and its low-cost, robust, and easy-to-realize structure make this antenna suitable for IoT applications.

INDEX TERMS Compact antennas, omnidirectional antennas, circular polarization, Internet-of-Things (IoT).

I. INTRODUCTION

AMONG the emerging technologies introduced by the Internet of Things (IoT), Machine-to-Machine (M2M) communications have attracted much interest during the last years [1], [2], [3]. In a context where the number of interconnected devices keeps increasing [4], the use of communications that do not involve human interaction becomes crucial. According to forecasts [5], the global market share for M2M solutions will keep growing by 20.5% until 2027 with industrial IoT applications taking the lead. Moreover, the demand for smaller, portable, and longer battery-life wireless devices drives this growth.

Antennas for IoT applications have to guarantee good all-around coverage in order to benefit portability, which is why dipole-like linearly polarized antennas have always been preferred [6], [7]. Recently, Omnidirectional Circularly Polarized (OCP) antennas have attracted more attention since they are effective in combating multi-path fading and do not require the same relative orientation between transmitting and receiving antennas [8]. OCP antennas can also enable more reliable communications that, thanks to the reduced number of packet re-transmissions, well fit the requirements of low-power IoT applications [9]. Their design, however, is not a trivial task, which is further complicated by the integration constraints of compact IoT devices.

In order to obtain a circular polarization (CP) while keeping a dipole-like (omnidirectional) radiation pattern, the E-field components E_θ and E_ϕ must have the same magnitude and a phase difference of odd multiples of 90° in each point of the azimuth plane [10].

In literature, different OCP antenna designs have been proposed over the years. In [11], using a coaxial cable for E_θ and a spiral slot over a surrounding shield for E_ϕ, a wideband flat OCP radiation with a 10.2 dBic maximum realized gain is obtained. However, the overall length of the structure (8.6λ) is not negligible. Similarly, surrounding a coaxial cable with radial CP loops [12], the profile of the antenna is reduced to 1.57λ keeping a high gain and wide bandwidth of 3.57%. In both cases, the use of the coaxial cable puts a strong constraint in terms of manufacturing and robustness

of the structure, but it develops a flat omnidirectional pattern, able to get high realized gain in the azimuth plane. A high gain can be also obtained by combining multiple OCP elements in arrays, as in [13], [14]. However, the size of these structures remains remarkable, and not suitable for IoT devices.

Lots of efforts have been done during these years to exploit CP on compact omnidirectional antennas [15], [16], [17], [18], [19], [20], [21], [22], [23], [24], [25], [26], [27], [28], [29]. The common theme to these designs is the composition of the CP as the combination of the two E-field components E_θ and E_ϕ generated by the compound of two antenna structures.

A combination of a slot and a modified PIFA is proposed in [15] at this scope. The need, however, for a fourfold parallel waveguide power divider and 90° phase shifter in the printed feeding network may be demanding to manufacture. A modified shorted patch and two strips, acting respectively as a magnetic and an electric source of current to develop an OCP radiation pattern are combined into a single structure in [16]. Even though the resulting antenna is easy to manufacture, the dimension of the strips ($\lambda/4$) implies an overall structure length of 1.8λ.

In [17], E_θ is excited by the TM_{01} mode of a Dielectric Resonator Antenna (DRA), while E_ϕ is due to the horizontal currents on logarithmic spiral slots in the ground plane. Similarly, in [18], E_θ is still generated by a DRA, while E_ϕ is provided by an Alford Loop (AL) placed on the top of the DRA. Despite the typical large bandwidth of DRAs, these antennas present a high profile compared to other solutions proposed in the literature.

Very low profile ($< 0.028\lambda$) antennas are obtained using a single-layer substrate circular patch that integrates vias responsible for the vertical E_θ component and slits that generate E_ϕ [19], [20], [21]. Similarly, the horizontal component can be induced from spiral slot shapes carved on a shorted patch radiator (responsible for the vertical E_θ component) [22], [23]. These antennas can provide a wide bandwidth ($>14.8\%$) but their surface is greater than $0.75 \times 0.75\lambda^2$ [20], [23]. Reducing the surface of this type of antenna would imply giving up on the bandwidth [19], [22]. A solution to reduce surface and keep a wide bandwidth is proposed in [21]. Increasing the volume of the antenna using stacked shorted patches with slits, a 32.5% usable bandwidth is obtained. However, the antenna section increases to half a wavelength.

Another way to generate the E_ϕ component is using sets of branches to compose horizontal dipoles, as in [24], [25], [26], where in both cases E_θ is due to vertical shorting pins. The $\lambda/2$ length of the branches in addition to the presence of a feeding line in [24] or a transmission line phase shifter in [25] impose a constraint on the antenna surface, which becomes greater than $0.6 \times 0.6\lambda$. A flexible structure is achieved in [26], by avoiding the presence of vertical pins (excluding the feeding one). Meandered lines are printed on the flexible substrate to well match with

the branch lines. However the size of the structure is still important ($0.55 \times 0.55 \times 0.2\lambda$).

In [27] the function of the branches is achieved by using 3D folded monopoles greatly reducing the overall antenna size $0.22 \times 0.22 \times 0.076\lambda^3$. However, despite the good performances in terms of bandwidth (3.89%) and gain (1.59dB), the structure may be fragile due to the unsupported metal wires acting as folded monopoles.

Another solution is to use two shorted parallel Printed Circuit Boards (PCBs) arranging the branches on a loop. As an example, the antenna proposed in [28] has an overall size that is remarkably small ($0.16\lambda \times 0.16\lambda \times 0.03\lambda$), but the usable bandwidth is narrow (only 0.9% at 1.435 GHz), and the combination between the orthogonal field components requires the integration of a feeding network. The use of a feeding network is avoided in [29] by properly selecting the distance between the vertical shorting vias and the feeding pin. The antenna combines a Zeroth-Order Resonator (ZOR) and a modified AL obtaining a 1.5 dBic maximum gain and 6% bandwidth at the cost of a larger size ($0.4\lambda \times 0.4\lambda \times 0.08\lambda$).

The combination of branches printed on two substrates to excite the E_ϕ component of the CP proposes a good trade-off between the overall antenna size and the CP performance, because, despite the use of two PCBs, the antenna profile remains relatively low (smaller than 0.08λ).

In this paper, a miniature OCP antenna suitable for low-cost low-power IoT devices is proposed. The antenna is based on an AL structure [30], which has been combined with a Wire-Patch (WP) structure to generate CP. This solution does not require expensive power dividers and power shifters to excite the two orthogonal electric field components. The antenna size is $0.25\lambda \times 0.25\lambda \times 0.08\lambda$ at 2.45 GHz and it is printed on two cost-effective FR4 PCBs. This work completes and extends a preliminary design presented in [31] by adding the detailed design process, the parametric analysis of the proposed antenna geometry, and the experimental characterization.

This paper is organized as follows. Section II reports the description of the antenna structure, the study of the main geometrical parameters involved in the antenna design process, and the analysis of the OCP composition. Section III presents the comparison between numerical and experimental results. Finally, conclusions are drawn in Section IV.
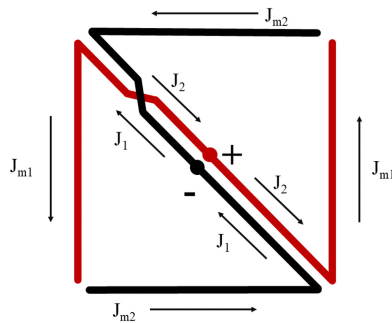
II. ANTENNA DESIGN
A. ANTENNA STRUCTURE

The proposed antenna (Fig. 1) is a combination of modified AL and WP structures that can excite both E_ϕ and E_θ components, respectively, for the CP polarization at 2.45 GHz.

It is made of two single-layer PCBs with a Z-shape on each outer face at distance $h = 10$ mm. The lower Z-shape is connected to the SMA connector shield, while the SMA core is connected to a 4 mm wide copper cylinder, which is, in turn, connected to the upper Z-shape. Both layers present
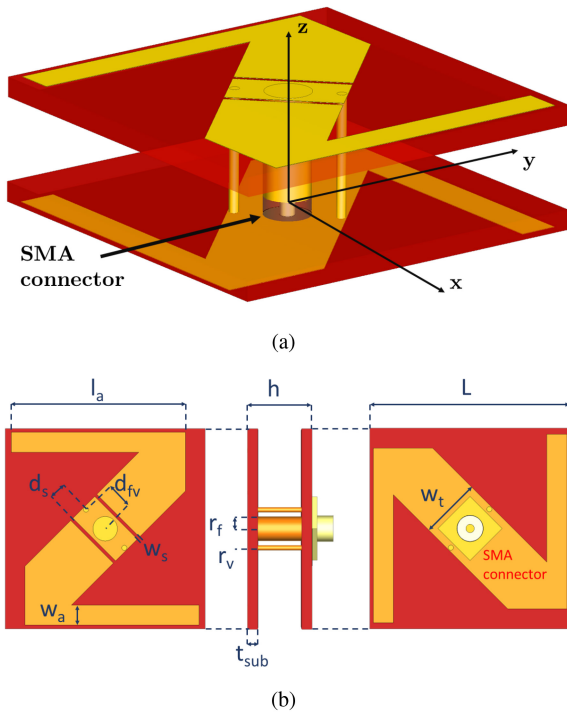
FIGURE 1. Structure of the proposed antenna with its fundamental parameters. (a) Perspective and (b) top, side, and bottom view projections.
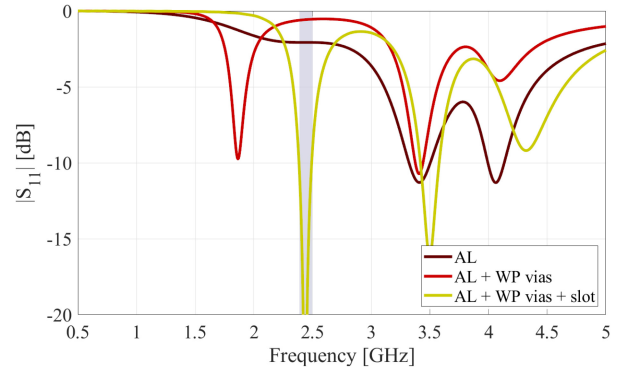

FIGURE 2. Theoretical current scheme of an AL antenna [30].

FIGURE 3. Antenna impedance matching behavior during the 3 main design steps with highlighted design band.

FIGURE 4. Design step #1: modified AL structure. (a)(c) $\theta = 90°$ E-field farfield cut [dB (V/m)] along with correspondent (b)(d) current distribution at (a)(b) 3.41 GHz and (c)(d) 4.1 GHz.
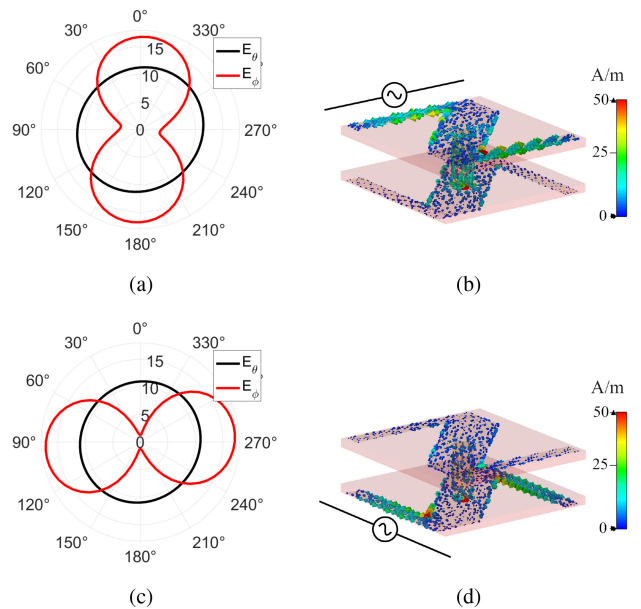
two shorting pins parallel to the central copper cylinder. Two slots are carved on the diagonal of the upper Z-shaped layer.

The proposed design is based on the structure introduced by Alford [30] whose theoretical current scheme is presented in Fig. 2, which provides an omnidirectional horizontally polarized far-field. Since currents $J_1 = J_2$ flows in opposite direction, the only constructive currents effects are given by the currents on the arms, namely J_m, that in fact compose the loop, with a current $J_{m1} = J_{m2}$.

The antenna design process relies on 3 main steps. First, a modified Z-shaped AL structure with coaxial feeding is inspected for the generation of E_ϕ. Then, vias are introduced parallel to the central feeding to realize a WP element and thus excite the E_θ component. Finally, slots are introduced in the Z-shaped AL upper layer to tune the E-field components to have the same magnitude at 2.45 GHz, thus enabling an OCP radiation behavior.

The modified two-layer Z-shaped AL structure can be seen as a combination of two folded dipoles in each layer. In order to ease the antenna manufacturing process, the SMA connector is soldered on the bottom layer, causing an asymmetry with respect to balanced resonant structures. As a matter of fact, the feeding point is located on the bottom layer, and the copper cylinder is therefore responsible for an increase of the electrical length of the upper layer. This emerges in Fig. 3 where simulated S-parameters of the three design steps are presented. For the AL case, the $|S_{11}|$ presents two minima, at 3.41 and 4.1 GHz. The farfield behavior in the azimuthal plane at these frequencies, shown in Fig. 4, confirms that the horizontal radiation is mainly driven by the folded dipole resonance, while the separation between the two peaks is given by the electrical length difference introduced by the feed.
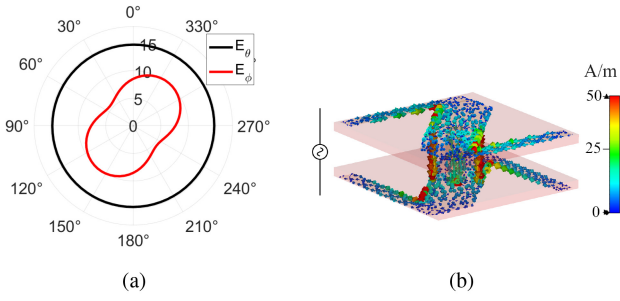
FIGURE 5. Design step #2: modified AL structure with vertical WP vias. (a) $\theta = 90°$ E-field farfield cut [dB (V/m)] along with correspondent (b) current distribution at 1.86 GHz.
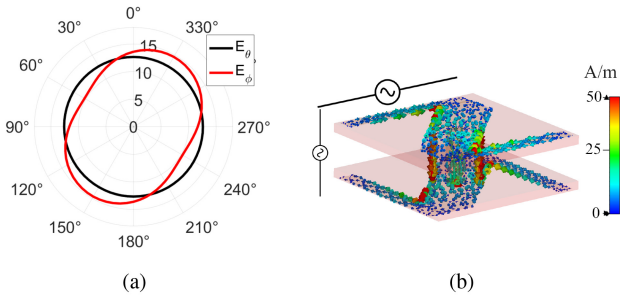

FIGURE 6. Design step #3: modified AL structure with vertical WP vias and slots. (a) $\theta = 90°$ E-field farfield cut [dB (V/m)] along with correspondent (b) current distribution at 2.44 GHz.

When vias are introduced to integrate the WP structure, another $|S_{11}|$ minimum appears at 1.86 GHz. As shown in Fig. 5, at this frequency the E_θ is excited by the current on the vias. This behavior was expected since, as in a typical WP structure [32], the two shorting wires between the two PCBs act as an equivalent parallel inductance to the capacitance made by the parallel printed Z-shapes. The resulting equivalent circuit allows the main currents to flow through the short circuit wires, which become responsible for the desired typical omnidirectional vertically polarized radiation pattern.

Finally, two slots are carved on the central trunk of the top Z-shaped strips. These slots represent an additional degree of freedom to find the proper balance between the AL and the WP radiation characteristics, and consequently, a good impedance matching in the desired band.

In Fig. 3, the peaks due to folded dipoles are still present and mainly unchanged. The first $|S_{11}|$ minimum responsible for the E_θ component instead is shifted to 2.45 GHz. Nevertheless, from Fig. 6 it appears that at this frequency the E_ϕ component is now excited too, with an elliptical shape due to the diagonal trunk, resulting in an overall azimuthal CP radiation behavior.

As an additional confirmation of this last statement, Fig. 7 shows the amplitude and phase of the E-field components in the azimuth plane ($\theta = 90°$) at 2.45 GHz. The well-balanced AL and WP sources of the antenna structure compose a stable 90° phase shift between the E_θ and E_ϕ across the whole azimuth plane. The oscillations on the
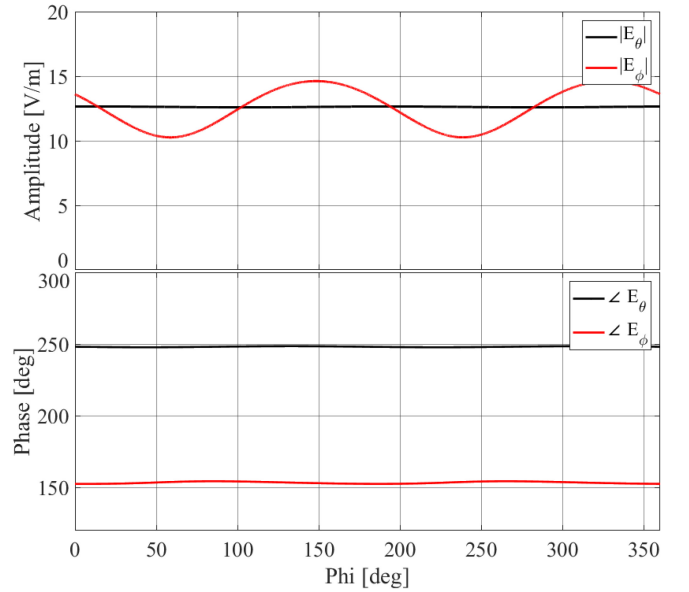
FIGURE 7. Amplitude and phase of E-field components across the azimuth $\theta = 90°$ plane.

E_ϕ amplitude component can be addressed to the elliptical shape of the E_ϕ component azimuthal cut. In Fig. 7, the RHCP is revealed due to the positive difference between E_θ and E_ϕ.
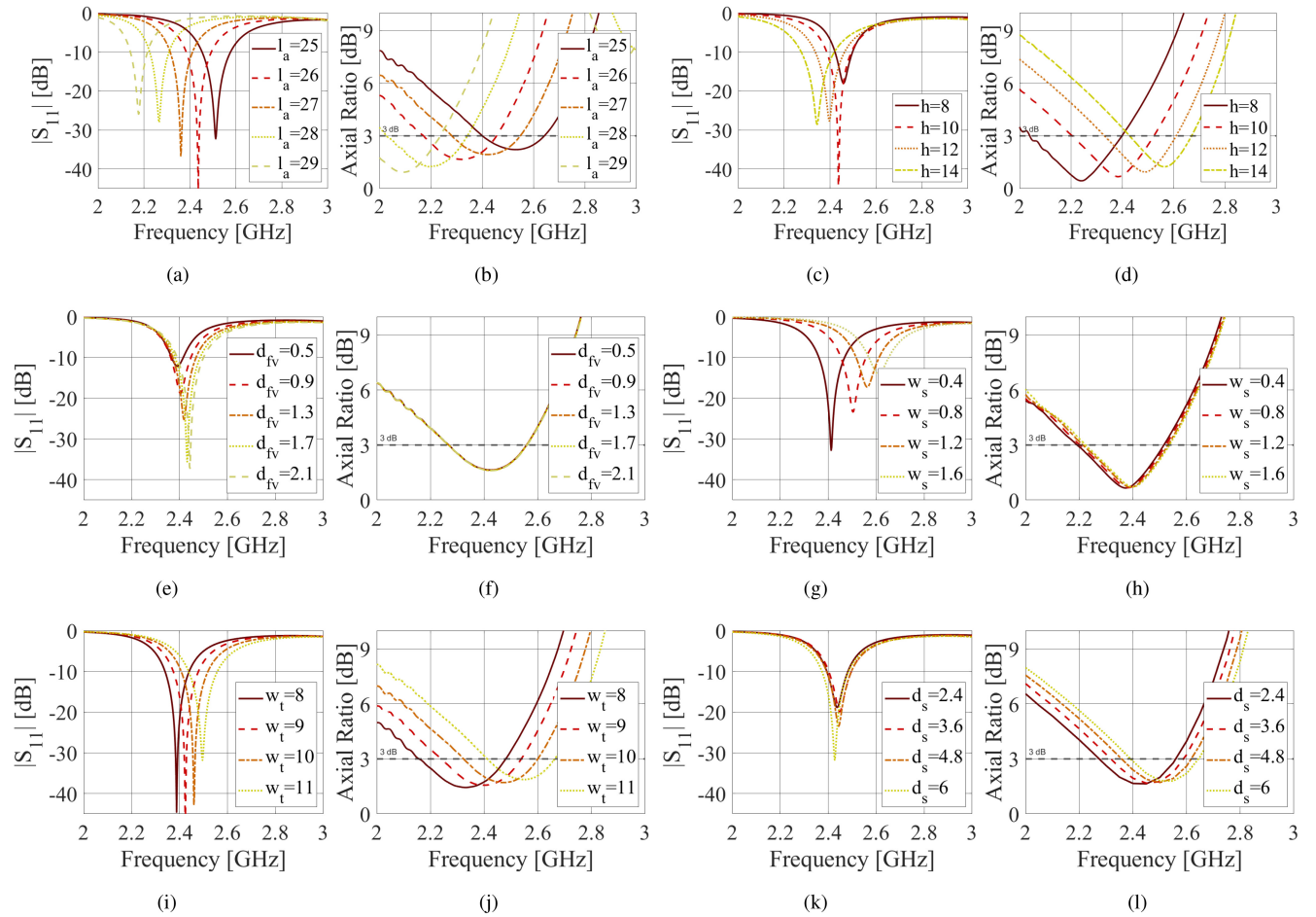
B. PARAMETERS OPTIMIZATION

All the antenna geometrical parameters have been optimized with the aim of obtaining a good impedance matching as well as a good CP level in the 2.4 GHz ISM band, i.e.,

$$\begin{cases} |S_{11}(f)| \leq -10 \text{ dB} \\ AR(f) \leq 3 \text{ dB} \end{cases} \quad 2.4 \leq f \leq 2.5 \text{ GHz.} \quad (1)$$

The optimization has been carried out through a parametric study, whose main results are reported in the following. Fig. 8 shows the effects of varying the main antenna geometrical parameters on both the $|S_{11}|$ and the AR. For each variation, the remaining geometrical parameters have been kept fixed to the values reported in Tab. 1.

The antenna resonance is mainly controlled by the length of the arms of the AL (l_a) and the distance between the top and bottom PCB layers (h). These two parameters are responsible for the antenna's overall horizontal and vertical extensions, respectively. Consequently, as their values increase (decrease), the antenna resonance shifts towards lower (higher) frequencies, as shown in Fig. 8(a) and Fig. 8(c). Concerning the AR, the variation of the antenna horizontal extension causes a frequency shift [Fig. 8(b)] that is in agreement with the one experienced by the $|S_{11}|$ parameter [Fig. 8(a)]. Differently, the effect of varying h on the AR is opposite [Fig. 8(d)] with respect to the one shown in Fig. 8(c). Varying the vertical extension of the antenna makes in fact varying both the inductive effect of the vias

FIGURE 8. Effects of varying the main antenna geometrical parameters on both the $|S_{11}|$ (left column) and AR (right column). All the values are in mm.

**TABLE 1.** Optimized antenna geometrical parameter values.

param. name	L	h	l_a	W_a	W_t	d_s	W_s	r_f	r_v	d_{fv}	t_{sub}
value [mm]	31	10	27	3.1	9.36	2.4	0.4	2	0.4	4.2	0.8

and the capacitive effect between the two PCBs, which are at the basis of the generation of the E_θ and the E_ϕ field components, respectively. Because of this behavior, the h parameter is fundamental to maximize the effectively usable bandwidth, which is the overlap between the impedance and the 3 dB AR bandwidths.

Concerning the impedance matching, this is mainly controlled by the radii of the short (r_v) and feeding (r_f) wires as well as by the short-feed distance (d_{fv}). As in a classical WP antenna, in fact, the proper design of the system composed by the feed and shorting wires allows the matching of the antenna input impedance to the port impedance, usually 50Ω. This is shown in Fig. 8(e), where the $|S_{11}|$ behavior for several d_{fv} values is reported. It must be pointed out that the variation of the short-feed distance has no effect on the CP [Fig. 8(f)].

Finally, as shown in Fig. 8(g), the width of slot cut (w_s) in the top z-shaped strip can be changed to fine tune the impedance matching, while the AR remains mostly unchanged [Fig. 8(h)]. On the other hand, the antenna AR can be optimized thanks to the width of the z-shape trunk and the slots' position, i.e., the length of the slot cut (w_t) and its distance from the center (d_s). These variations affect more the AR frequency shift [Figs. 8(j), 8(l)] rather than the resonance frequency shift [Figs. 8(i), 8(k)]. As a matter of fact, the balance between the amplitude of the horizontal currents flowing on the z-shaped strips and the vertical currents flowing on the vias can be controlled by varying the position, length and width of the slot.

Based on this parametric analysis, the antenna optimization process was as follows. It first started with changing the AL arms' length l_a and PCB layers distance h to obtain a proper resonance and a low AR in the required frequency range. Successively, the optimal d_{fv} value was found, and finally, fine-tuning was performed by changing the trunk width w_t, the slot width w_s and position d_s. The final antenna geometrical parameter values are reported in Tab. 1.
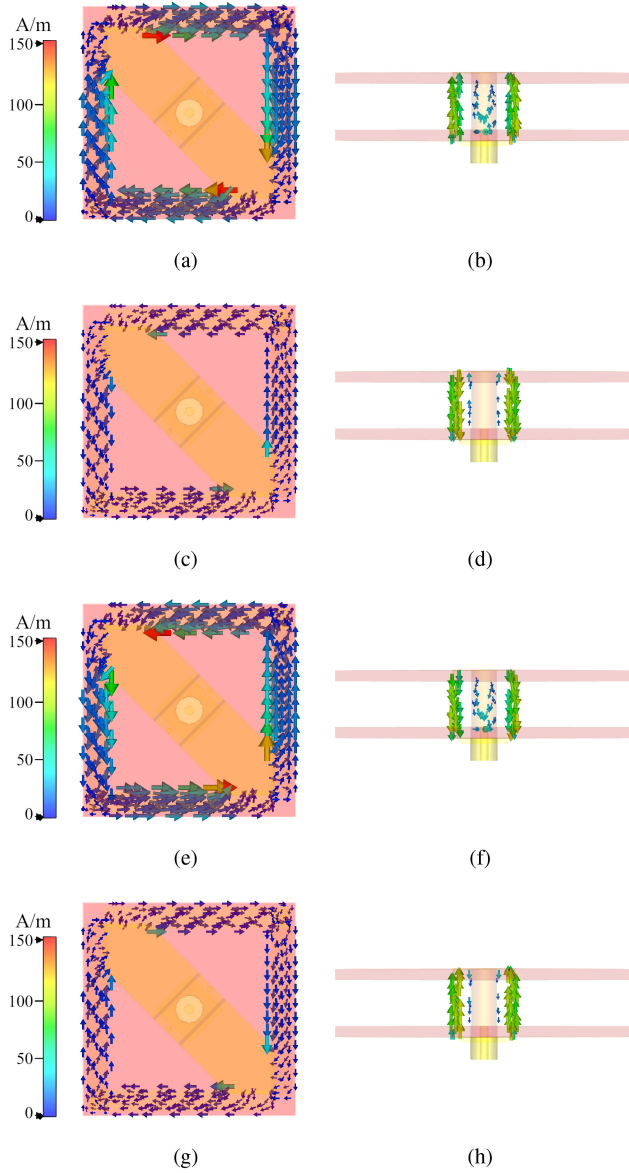
FIGURE 9. Surface current for *t* = 0 (a), (b), *t* = *T*/4 (c), (d), *t* = *T*/2 (e), (f) and *t* = 3*T*/4 (g), (h), on the Loop (left) and WPA vias (right) from bottom and side views, respectively.

C. CIRCULAR POLARIZATION ANALYSIS

In order to verify the CP mechanism as a combination of horizontally and vertically polarized sources, Fig. 9 shows the current distribution from bottom and side view respectively, for 4 equally-spaced time instants $t = nT/4$, $n = 0, 1 \cdots 3$, T being the period at $f = 2.45$ GHz. Currents on the diagonal trunk are hidden for the sake of clarity, since it has been already showed how currents in the feeding lines of an AL offset each other in Fig. 2 and [31].

Fig. 9(a) shows a strong clockwise current flowing at $t = 0$. In opposition, at the same time instant, the profile view in Fig. 9(b) shows a moderate intensity of current on the vias flowing from the lower PCB to the upper one. At this instant, the AL radiation, thus the horizontal E_ϕ component, is dominant compared to the WP one.
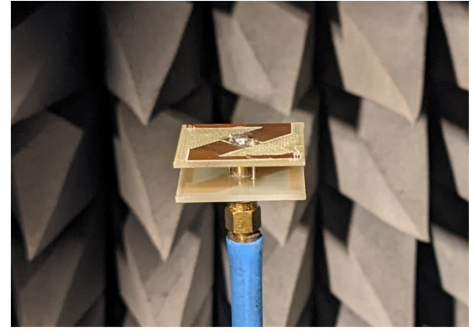
FIGURE 10. Antenna prototype during the measurements in the SATIMO Starlab system.

In Fig. 9(c) the current on the AL arms at $t = T/4$ is weaker than the one at the previous time instant. Fig. 9(d) instead shows an increase of current intensity on vias, meaning that now the vertical component becomes dominant compared to the horizontal one generated by the loop. Both currents flows in opposite direction compared to the previous case.

At $t = T/2$, the amplitude of the current flowing on the loop increases without changing its counterclockwise direction, as shown in Fig. 9(e). Current on vias in Fig. 9(f) keeps its direction but becomes weaker. Again, the AL-generated E_ϕ component becomes dominant over E_θ.

Finally, at $t = 3T/4$, the current flow over the AL arms changes its direction to clockwise again and gets weaker in Fig. 9(g). As a consequence the current on vias in Fig. 9(h) changes its direction too and increases in intensity.

Based on such an analysis, we can affirm that the E_ϕ and E_θ components are 90° phased shifted by each other. As a matter of fact, each maximum (minimum) current intensity on vias is delayed by $T/4$ with respect to each current maximum (minimum) intensity on the AL arms.

III. NUMERICAL AND EXPERIMENTAL RESULTS

The effectiveness of the proposed antenna has been numerically and experimentally assessed. All the simulations have been carried out using CST microwave studio electromagnetic simulator. As for the measurements, a prototype of the proposed antenna has been realized (Fig. 10). The two PCBs have been printed using a photolithographic process, and successively soldered to the vias with the help of a low-cost 3D printed PLA removable structure, which guaranteed the distance between layers and the accurate positioning of the vias. The S_{11} parameter was measured with a Keysight Vector Network Analyzer (VNA), while the radiation patterns were measured with a SATIMO Starlab system.

The comparison between simulated and measured values for both $|S_{11}|$ and Total Efficiency is shown in Fig. 11. The antenna exhibits a good impedance matching in the desired band, with a simulated -10 dB matching band ranging from 2.38 to 2.49 GHz (4.6%). Measurements are in good agreement with the simulations, with the $|S_{11}| \leq -10$ dB from 2.4 to 2.52 GHz (4.2%), thus covering the entire 2.4-2.5 GHz ISM band.
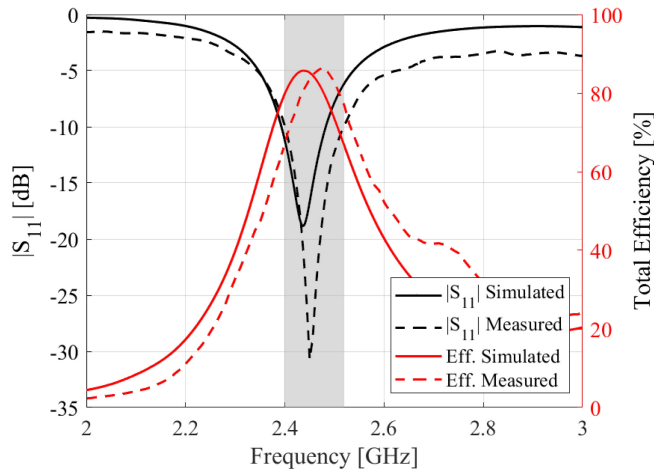
FIGURE 11. Simulated and measured antenna $|S_{11}|$ and total efficiency.

Despite the small dimensions, the antenna presents a simulated maximum total efficiency of 87% at 2.45 GHz, while the measured one is 86% at 2.48 GHz. The small frequency shift (only 1.6%), as in the case of the S_{11} parameter in Fig. 11, can be ascribed to small imperfections in the realization of the prototype. Nevertheless, the measured antenna total efficiency is always higher than 70% all over the 2.4-2.5 GHz ISM band.

Finally, Fig. 12 shows the simulated and measured antenna realized gain and AR patterns in both the azimuth and elevation planes at 2.45 GHz. The patterns are shown in terms of RHCP and LHCP gain components. In the azimuth plane, the simulated RHCP component is always at least 15 dB higher than the LHCP one. The shapes of the radiation pattern in the planes at $\theta = 90°$ [Fig. 12(a)], $\phi = 0°$ [Fig. 12(c)], and $\phi = 90°$ [Fig. 12(e)] confirm that the antenna exhibits a classical dipole-like RHCP behavior with an omnidirectional radiation behavior in the azimuth plane.

The elliptical shape of the RHCP radiation pattern is due to the intrinsic asymmetry of the antenna structure. The AL geometry used to excite the horizontally polarized radiation component consists of two Z-shaped metallic layers that are aligned only along one diagonal direction so that the currents at the center of the structure can cancel each other. Moreover, even the vias are placed along only one diagonal, thus further increasing the asymmetry of the antenna structure. As a result, the RHCP gain values are minimum (-0.24 dBic) at $\phi = 60°$ and $\phi = 240°$, and maximum (1.91 dBic) at $\phi = 150°$ and $\phi = 330°$.

Finally, it must be pointed out that measurements and simulations of the RHCP component are in very good agreement [black curves in Figs 12(a), 12(c), and 12(e)]. Larger differences between simulated and measured curves are visible for the LHCP component [red curves in Figs 12(a), 12(c), and 12(e)]. This is due to the fact that the small values of the LHCP component, i.e., the cross-polar component [always less than -10 dB in Fig. 12(a), and always less than -15 dB in Figs. 12(c), and 12(e)] suffer more from the imperfections
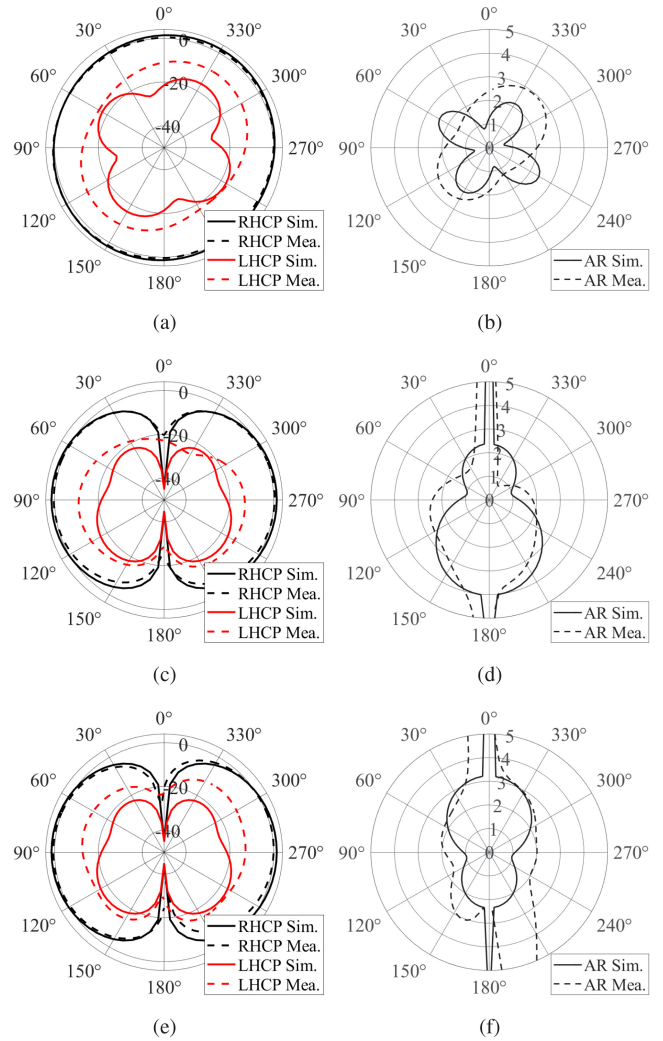

FIGURE 12. Simulated and measured antenna RHCP and LHCP realized gain (left) and AR (right) patterns in planes at $\theta = 90°$ (a), (b), $\phi = 0°$ (c), (d), and $\phi = 90°$ (e), (f).

of the prototype and from the accuracy of the measurement system.

On the right column of Fig. 12, the AR further confirms the OCP radiation. Both the simulated and the measured AR values are always lower than 3 dB across the azimuth plane [Fig. 12(b)]. In the elevation planes [Fig. 12(d) and Fig. 12(f)], the AR is always lower than 3 dB in the range between $\theta = 20°$ and $\theta = 135°$, confirming that the RHCP is preserved over a vertical beamwidth of 115°. Also in this case, measured values are in good agreement with the numerical ones. As the AR results are calculated from the simulated and measured RHCP and LHCP components, their differences are a direct consequence of the differences between simulated and measured gain values (mainly LHCP).

IV. CONCLUSION

In this paper, a compact OCP antenna has been presented. The RHCP radiation behavior has been obtained thanks to the proper integration of an AL and a WP antenna structures. A

TABLE 2. Comparison of the main OCP antenna solutions available in literature.

Ref	Type	Frequency [GHz]	Usable BW* [$\% / GHz$]	Size [λ]	Gain [$dBic$]	Efficiency [$\%$]
[16]	$\lambda/4$ shorted patch	5.8	$4.3 / (5.63 - 5.88)$	$1.8 \times 0.32 \times 0.04$	3	70
[17]	DRA + Spiral Slots	2.44	$7 / (2.35 - 2.52)$	$0.5 \times 0.5 \times 0.17$	1.3	87
[18]	DRA + Alford Loop	2.44	$7 / (2.34 - 2.51)$	$0.38 \times 0.38 \times 0.18$	1.8	93
[19]	shorts + V slits	5.8	$3.5 / (5.65 - 5.85)$	$0.52 \times 0.52 \times 0.026$	1.26	90
[20]	shorts + slits	2.4	$14.8 / (2.26 - 2.62)$	$0.75 \times 0.75 \times 0.028$	0.7	72
[21]	shorts + slits	1.385	$32.5 / (1.16 - 1.61)$	$0.34 \times 0.34 \times 0.5$	2.1	85
[22]	shorts + spiral slot	1.65	$0.48 / (1.646 - 1.654)$	$0.33 \times 0.33 \times 0.017$	0.1	68
[23]	shorts + spiral slot	2.73	$51.7 / (2.11 - 3.58)$	$0.85 \times 0.85 \times 0.14$	1	/
[24]	shorts + arc dipoles	1.95	$25.6 / (1.7 - 2.2)$	$0.61 \times 0.61 \times 0.066$	-1.12	/
[25]	shorts + branches	5.8	$4 / (5.68 - 5.91)$	$0.62 \times 0.62 \times 0.03$	1.77	97
[26]	feed pin + branches	5.8	$2.9 / (5.72 - 5.89)$	$0.55 \times 0.55 \times 0.2$	2.1	73
[27]	folded monopoles	2.44	$3.9 / (2.395 - 2.49)$	$0.22 \times 0.22 \times 0.076$	1.59	/
[28]	shorts + loop	1.435	$0.9 / (1.429 - 1.442)$	$0.16 \times 0.16 \times 0.03$	1.01	/
[29]	ZOR + loop	2.44	$6.1 / (2.38 - 2.53)$	$0.4 \times 0.4 \times 0.08$	1.95	/
This work	WP + AL	2.45	$4.9 / (2.4 - 2.52)$	$0.25 \times 0.25 \times 0.08$	1.91	87

*The usable bandwidth (BW) is defined as the overlap between the $|S_{11}| \leq -10$ dB and the $AR \leq 3$ dB antenna frequency bands.

prototype of the antenna has been fabricated and tested. The measured results are in good agreement with the simulated ones and confirm the effectiveness of the proposed solution in terms of both electrical and radiation characteristics.

Compared to the main alternative OCP antenna solutions available in the literature (Tab. 2), the antenna proposed in this paper presents a good trade-off between dimensions and performance. The antenna size is, in fact, a key parameter as antennas with small dimensions are better candidates for integration in compact IoT devices. As shown in Tab. 2, using branches or loops as antenna components (as done in this work and in [24], [25], [26], [27], [28], [29]) has demonstrated to be, in general, more efficient in terms of surface size compared to the use of patch slits [19], [20], [21] or spiral slots [22], [23], and for reduced antenna profile compared to DRAs [17], [18]. More specifically, only the antennas presented in [27], [28] are smaller (in terms of surface) than the solution proposed in this paper, but at the cost of a strong performance reduction.

Comparing this work's antenna to those of the same type [24], [25], [26], [27], [28], [29], the solution presented in [24] exhibits a much wider bandwidth (25.6% vs. 4.9%), but its planar extension is almost 6 times bigger and its gain is 3 dB lower. The solution reported in [25] is much thinner than our work (0.03λ vs. 0.08λ), but, again, its surface is more than 6 times larger, and both the gain and the usable bandwidth are slightly lower. The work in [26] presents similar radiation performance with a 2.1 dBi gain, but its volume is 12 times bigger and its usable bandwidth is thinner (2.9% vs. 4.9%). Differently, the solution presented in [27] has similar dimensions, but a smaller usable bandwidth (3.9% vs. 4.9%), and a lower maximum azimuthal realized gain (1.59 dBic vs. 1.91 dBic). Compared to the work in [28], the antenna proposed here is 1.56 times larger and 2.67

times thicker. However, its bandwidth is 5 times wider (to cover the entire 2.4-2.5 ISM band) and its gain is 1.89 times higher. Finally, the work in [29] exhibits a 1.2 larger usable fractional bandwidth at the cost of a 1.6 larger planar extension and for similar values of the realized gain (1.91 vs. 1.95 dBic).

In conclusion, thanks to its smaller dimensions, the design proposed in this paper better fits the size constraints of modern IoT devices, while still being able to cover the entire 2.4-2.5 GHz ISM band with good efficiency and gain values. Moreover, The use of low-cost materials, the simplicity of realization, and the robustness of the structure make the proposed antenna ideal for large-scale IoT application scenarios.

REFERENCES

[1] M. A. G. Ghasri and A. M. A. Hemmatyar, "A new dynamic optimal M2M RF interface setting in relay selection algorithm (DORSA) for IoT applications," *IEEE Access*, vol. 10, pp. 5327–5342, 2022.

[2] N. S. Chilamkurthy, O. J. Pandey, A. Ghosh, L. R. Cenkeramaddi, and H.-N. Dai, "Low-power wide-area networks: A broad overview of its different aspects," *IEEE Access*, vol. 10, pp. 81926–81959, 2022.

[3] N. Ahmed, D. De, F. A. Barbhuiya, and M. I. Hussain, "MAC protocols for IEEE 802.11ah-based Internet of Things: A survey," *IEEE Internet Things J.*, vol. 9, no. 2, pp. 916–938, Jan. 2022.

[4] B. Heslop, "By 2030, each person will own 15 connected devices. Here's what that means for your business and content." 2021. [Online]. Available: https://www.spiceworks.com/marketing/iot-in-marketing/articles/by-2030-each-person-will-own-15-connected-devices-heres-what-that-means-for-your-business-and-content/

[5] "Cellular M2M market report." ResearchDive. 2021. [Online]. Available: https://www.researchdive.com/5826/cellular-m2m-market

[6] J. Jeon, K. Jang, S. Kahng, and C. Park, "Design of a miniaturized UHF-band Zigbee antenna applicable to the M2M/IoT communication," in *Proc. IEEE Antennas Propag. Soc. Int. Symp. (APSURSI)*, 2014, pp. 382–383.

[7] M. Sumi and Y. Suzuki, "A wideband single-sided folded-off-center-fed dipole antenna for 4G/5G/Wi-Fi M2M/IoT applications and UAVs," in *Proc. IEEE Conf. Antenna Meas. Appl. (CAMA)*, 2021, pp. 3–4.

[8] S. Gao, Q. Luo, and F. Zhu, *Circularly Polarized Antennas*. Chichester, U.K.: IEEE Press/Wiley, 2014.

[9] Y. Wang, *Omnidirectional Circularly Polarized Antenna*. Boston, MA, USA: De Gruyter, 2021, ch. 9, pp. 296–318.

[10] C. A. Balanis, *Antenna Theory: Analysis and Design*, 4 ed. Hoboken, NJ, USA: Wiley, 2016.

[11] G. Zheng and B. Sun, "High-gain normal-mode omnidirectional circularly polarized antenna," *IEEE Antennas Wireless Propag. Lett.*, vol. 17, no. 6, pp. 1104–1108, Jun. 2018.

[12] X. Quan, R. Li, and M. M. Tentzeris, "A broadband omnidirectional circularly polarized antenna," *IEEE Trans. Antennas Propag.*, vol. 61, pp. 2363–2370, May 2013.

[13] W. Lin and R. W. Ziolkowski, "Compact, high directivity, omnidirectional circularly polarized antenna array," *IEEE Trans. Antennas Propag.*, vol. 67, no. 7, pp. 4537–4547, Jul. 2019.

[14] J. Shi, X. Wu, X. Qing, and Z. N. Chen, "An omnidirectional circularly polarized antenna array," *IEEE Trans. Antennas Propag.*, vol. 64, no. 2, pp. 574–581, Feb. 2016.

[15] J. Wu and K. Sarabandi, "Compact omnidirectional circularly polarized antenna," *IEEE Trans. Antennas Propag.*, vol. 65, no. 4, pp. 1550–1557, Apr. 2017.

[16] J. Liu, Y. Li, Z. Liang, and Y. Long, "A planar quasi-magnetic–electric circularly polarized antenna," *IEEE Trans. Antennas Propag.*, vol. 64, no. 6, pp. 2108–2114, Jun. 2016.

[17] N. Yang, K. W. Leung, K. Lu, and N. Wu, "Omnidirectional circularly polarized dielectric resonator antenna with logarithmic spiral slots in the ground," *IEEE Trans. Antennas Propag.*, vol. 65, no. 2, pp. 839–844, Feb. 2017.

[18] W. W. Li and K. W. Leung, "Omnidirectional circularly polarized dielectric resonator antenna with top-loaded Alford loop for pattern diversity design," *IEEE Trans. Antennas Propag.*, vol. 61, no. 8, pp. 4246–4256, Aug. 2013.

[19] C. Guo, R. Yang, and W. Zhang, "Compact omnidirectional circularly polarized antenna loaded with complementary V-shaped slits," *IEEE Antennas Wireless Propag. Lett.*, vol. 17, no. 9, pp. 1593–1597, Sep. 2018.

[20] Y. Shi and J. Liu, "Wideband and low-profile omnidirectional circularly polarized antenna with slits and shorting-vias," *IEEE Antennas Wireless Propag. Lett.*, vol. 15, pp. 686–689, 2016.

[21] M. Akmal, A. Alieldin, and A. R. Eldamak, "A high-power sandwiched omnidirectional circularly polarized antenna for GNSS systems," *IEEE Access*, vol. 11, pp. 31167–31176, 2023.

[22] D. Yu, S.-X. Gong, Y.-T. Wan, and W.-F. Chen, "Omnidirectional dual-band dual circularly polarized microstrip antenna using tm_{01} and tm_{02} modes," *IEEE Antennas Wireless Propag. Lett.*, vol. 13, pp. 1104–1107, 2014.

[23] D. Yu, S.-X. Gong, Y.-T. Wan, Y.-L. Yao, Y.-X. Xu, and F.-W. Wang, "Wideband omnidirectional circularly polarized patch antenna based on vortex slots and shorting vias," *IEEE Trans. Antennas Propag.*, vol. 62, no. 8, pp. 3970–3977, Aug. 2014.

[24] Y. Ma, J. Li, and R. Xu, "Design of an omnidirectional circularly polarized antenna," *IEEE Antennas Wireless Propag. Lett.*, vol. 16, pp. 226–229, 2017.

[25] Q.-X. Chu, M. Ye, and X.-R. Li, "A low-profile omnidirectional circularly polarized antenna using planar sector-shaped endfire elements," *IEEE Trans. Antennas Propag.*, vol. 65, no. 5, pp. 2240–2247, May 2017.

[26] X. Hu, S. Yan, J. Zhang, V. Volski, and G. A. E. Vandenbosch, "Omni-directional circularly polarized button antenna for 5 GHz WBAN applications," *IEEE Trans. Antennas Propag.*, vol. 69, no. 8, pp. 5054–5059, Aug. 2021.

[27] Y. Yu, Z. Shen, and S. He, "Compact omnidirectional antenna of circular polarization," *IEEE Antennas Wireless Propag. Lett.*, vol. 11, pp. 1466–1469, 2012.

[28] D. Wu, X. Chen, L. Yang, G. Fu, and X. Shi, "Compact and low-profile omnidirectional circularly polarized antenna with four coupling arcs for UAV applications," *IEEE Antennas Wireless Propag. Lett.*, vol. 16, pp. 2919–2922, 2017.

[29] L. Yang, N.-W. Liu, Z.-Y. Zhang, G. Fu, Q.-Q. Liu, and S. Zuo, "A novel single feed omnidirectional circularly polarized antenna with wide AR bandwidth," *Progr. Electromagn. Res. C*, vol. 51, pp. 35–43, Jun. 2014.

[30] A. Alford and A. G. Kandoian, "Ultrahigh-frequency loop antennas," *Electr. Eng.*, vol. 59, no. 12, pp. 843–848, 1940.

[31] V. Mastrosimini, L. Santamaria, M. Grande, F. Ferrero, R. Staraj, and L. Lizzi, "Miniaturized omnidirectional circularly polarized antenna for IoT applications," in *Proc. 15th Eur. Conf. Antennas Propag. (EuCAP)*, 2021, pp. 1–4.

[32] C. Delaveaud, P. Leveque, and B. Jecko, "New kind of microstrip antenna: The monopolar wire-patch antenna," *Electron. Lett.*, vol. 30, no. 1, pp. 1–2, Jan. 1994.

FRANCESCO POSITANO (Graduate Student Member, IEEE) received the M.Sc. degree in telecommunications engineering from the Politecnico di Bari, Bari, Italy, in 2021. He is currently pursuing the Ph.D. degree with the Laboratory of Electronics, Antennas and Telecommunications, Univerisité côte d'Azur, Sophia Antipolis, France. His current research interests include miniature, low power and reconfigurable antennas for Internet of Things applications.

LUCA SANTAMARIA (Member, IEEE) received the first M.Sc. degree in computer science from the Université Côte d'Azur, Sophia Antipolis, France, the second M.Sc. degree in telecommunications engineering from the Politecnico di Bari, Bari, Italy, in 2018, and the Ph.D. degree from the Laboratory of Electronics, Antennas, and Telecommunications, Université Côte d'Azur in 2021, working in the field of low-power reconfigurable antennas for IoT and 5G communications.

ROBERT STARAJ (Member, IEEE) was born in Antibes, France, in 1965. He received the Ph.D. degree in electronics from University Nice-Sophia Antipolis, France, in 1992. In 1993, he joined the Ecole Supérieure d'Ingénieurs de Nice-Sophia Antipolis and the Laboratory of Electronics, Antennas and Télécommunications (LEAT)-CNRS UMR7248 as an Assistant Professor. Since 2003, he has been a Full Professor with the Polytech'Nice-Sophia, Ecole Polytechnique de l'Université de Nice-Sophia, and In-Charge of the Telecommunications and Networks speciality of the Electronics Department. He was the Director of the GDR Ondes-CNRS, French National Research Group on Waves from 2014 to 2017 and the Assistant Director of LEAT. After being the head of the Conception et Modélisation d'Antennes—Antennas Design and Modeling, LEAT during several years, he is currently the Director of LEAT. His research focuses on printed antennas and arrays, active, integrated, adaptative, and miniature multistandard antennas for wireless, RFID, MIMO systems, and biomedical applications.

LEONARDO LIZZI (Senior Member, IEEE) received the master's degree in telecommunication engineering and the Ph.D. degree in information and communication technology from the University of Trento, Italy, in 2007 and 2011, respectively. He is currently an Associate Professor with the University Côte d'Azuri, France. During his Ph.D., he has been a Visiting Researcher with The Pennsylvania State University, USA, and the University of Nagasaki, Japan. From 2011 to 2014, he was Postdoctoral Researcher with the Laboratory of Electronics, Antennas and Telecommunications, UCA. He is the coordinator of the European School of Antennas Ph.D. course on "Antennas and Rectennas for IoT Applications." He is the coauthor of more than 140 papers in international journals and conference proceedings. At the moment, his research focuses on reconfigurable, miniature, multi-standards antennas for Internet-of-Things applications, wearable devices and 5G terminals.